Check for updates

Advanced Functional Materials

ADVANCED FUNCTIONAL MATERIALS
www.afm-journal.de

RESEARCH ARTICLE OPEN ACCESS

Vector-Field Control and Emergent Basal-Plane Anisotropy of Magnetic Textures in Noncentrosymmetric $(Fe_{0.63}Ni_{0.3}Pd_{0.07})_3P$

Victor Ukleev[1] | Oleg I. Utesov[2,3] | Lorenzo Ubilla[1] | Chen Luo[1] | Radu-Marius Abrudan[1] | Peter Wild[4] | Holger Kropf[1] | Moritz Winter[5,6] | Sebastian Schneider[6] | Alexander Tahn[6] | Bernd Rellinghaus[6] | Tim A. Butcher[7] | Simone Finizio[8] | Sebastian Wintz[1] | Markus Weigand[1] | Max T. Birch[9] | Yoshinori Tokura[9,10,11] | Yasujiro Taguchi[9,12] | Kosuke Karube[9] | Florin Radu[1]

[1]Helmholtz-Zentrum Berlin für Materialien und Energie, Berlin, Germany | [2]Department of Physics, Korea Advanced Institute of Science and Technology, Daejeon, Republic of Korea | [3]Center for Theoretical Physics of Complex Systems, Institute for Basic Science (IBS), Daejeon, Republic of Korea | [4]Heinz Maier-Leibnitz Zentrum (MLZ), Technische Universität München, Garching, Germany | [5]Max Planck Institute for Chemical Physics of Solids, Dresden, Germany | [6]Dresden Center for Nanoanalysis, cfaed, Technical University Dresden, Dresden, Germany | [7]Max Born Institute for Nonlinear Optics and Short Pulse Spectroscopy, Berlin, Germany | [8]Swiss Light Source, Paul Scherrer Institut, Villigen PSI, Switzerland | [9]RIKEN Center for Emergent Matter Science (CEMS), Wako, Japan | [10]Department of Applied Physics, University of Tokyo, Tokyo, Japan | [11]Tokyo College, University of Tokyo, Tokyo, Japan | [12]Baton Zone Program (BZP), TRIP Headquarters, RIKEN, Japan

Correspondence: Victor Ukleev (victor.ukleev@helmholtz-berlin.de)

Received: 20 March 2026 | **Revised:** 23 June 2026 | **Accepted:** 4 August 2026

Keywords: anisotropy | condensed matter physics | Dzyaloshinskii–Moriya interaction | magnetocrystalline anisotropy | ptychography | soft x-ray scattering | skyrmions | stripe domains

ABSTRACT

$(Fe_{0.63}Ni_{0.3}Pd_{0.07})_3P$ is a room-temperature magnet with S_4 symmetry that hosts a rich variety of topological spin textures. Here, we report a combined resonant small-angle x-ray scattering and ptychography study of $(Fe_{0.63}Ni_{0.3}Pd_{0.07})_3P$ in vector magnetic fields over a broad temperature range. We demonstrate deterministic vector-field control of magnetic stripe domains, where in-plane fields continuously rotate their orientation via a transition from a chiral stripe to an achiral fan configuration. Furthermore, at 50 K and below, the stripe orientation becomes metastably pinned and retains its field-trained direction. While the magnitude of the wavevector is nearly isotropic within the basal plane at room temperature, a pronounced temperature evolution of anisotropic interactions emerges upon cooling. In particular, non-trivial anisotropy axes develop at 20–50 K reflecting the combined effects of magnetocrystalline anisotropy, anisotropic exchange, and Dzyaloshinskii–Moriya interaction (DMI), whose effective orientation is found to rotate with temperature. These results establish $(Fe_{0.63}Ni_{0.3}Pd_{0.07})_3P$ as a model system for vector-field control of chiral spin textures and reveal a previously unrecognized temperature-driven evolution of the effective DMI landscape in a noncentrosymmetric magnet.

1 | Introduction

Noncentrosymmetric magnets with competing symmetric and antisymmetric exchange interactions provide fertile ground for the stabilization of complex spin textures such as helices, conical spirals, and skyrmion lattices [1, 2]. In such systems, the absence of inversion symmetry allows for a Dzyaloshinskii–Moriya interaction (DMI) [3, 4] that controls the rotational sense of the magnetization and competes with the exchange and anisotropy terms to produce long-periodic, modulated ground-state spin

This is an open access article under the terms of the Creative Commons Attribution License, which permits use, distribution and reproduction in any medium, provided the original work is properly cited.
© 2026 The Author(s). *Advanced Materials* published by Wiley-VCH GmbH

structures. The direction and symmetry of these modulations are essentially governed by the crystallographic class: for example, chiral cubic compounds host isotropic DMI leading to Bloch-type skyrmion lattices [5, 6], whereas polar, D_{2d} and S_4 systems exhibit anisotropic Dzyaloshinskii–Moriya (DM) vectors that confine the propagation vectors to a high-symmetry crystallographic plane and stabilize Néel-type skyrmions [7, 8] and antiskyrmions [9, 10], respectively. However, the role of in-plane vector magnetic fields in controlling propagation vectors of magnetic textures in S_4-symmetric magnets remains poorly understood.

Recently, two families of tetragonal compounds have attracted attention for hosting room-temperature antiskyrmions. The first, which includes Heusler alloys $Mn_{1.4}Pt_{0.9}Pd_{0.1}Sn$ and $Mn_{1.4}PtSn$ (hereafter we only focus on the representative member $Mn_{1.4}PtSn$ referred to as MPS), possesses D_{2d} symmetry [9], while the second, Pd-doped schreibersites, represented by $(Fe_{0.63}Ni_{0.3}Pd_{0.07})_3P$ (hereafter FNPP), belongs to the S_4 class [10, 11]. FNPP crystallizes in a noncentrosymmetric structure with space group $I\bar{4}$, where Fe, Ni, and Pd atoms occupy three inequivalent Wyckoff positions, giving rise to anisotropic DMI confined within the basal plane. In contrast to D_{2d}, S_4 symmetry lacks mirror planes but retains a fourfold rotoinversion axis, resulting in a distinct set of DM vectors with mixed in-plane and out-of-plane components. In theory, this lower symmetry allows for more complex chiral modulations, including both Bloch-type helical and Néel-type cycloidal textures [2, 12]. Additionally, in bulk MPS and FNPP, a strong uniaxial anisotropy and long-ranged magnetic dipole-dipole interaction [10, 13] dominate over DMI-induced topological spin textures and stabilize long-scale (tens of microns) fractal domain patterns in thick samples [14, 15]. We emphasize that due to the minor role of DMI in these two material systems, it is more appropriate to assign their ground state to a stripe domain phase [16] rather than a helical spiral state typical to archetype chiral magnets such as MnSi [1]. In this context, the stripe-domain states realized in FNPP can be viewed as a limiting case of a π-rotation chiral soliton lattice (π-CSL) in the weak-DMI regime, providing a natural bridge between dipolar-driven magnetic domains and chiral soliton physics [17].

Unlike MPS, where the zero-field Bloch-type stripe domain texture propagates along the ⟨100⟩ axes, they orient preferably along the ⟨110⟩ diagonals in FNPP, due to the combined effects of easy-axis and basal anisotropies as well as the anisotropic DMI [18, 19].

Despite extensive investigations of the topology pertaining to the magnetic structures in these antiskyrmion hosts, key aspects related to detailed conditions for stabilization of diverse chiral magnetic structures remain unresolved. While the bulk magnetic properties of cubic chiral Bloch-type and polar Néel-type skyrmion hosts are well studied by small-angle neutron scattering (SANS) [20], this approach is less effective for MPS and FNPP due to the large size of magnetic domains in bulk crystals [14, 15]. Consequently, most studies on these materials have relied on Lorentz transmission electron microscopy (LTEM) of thin lamellae. LTEM offers nanometric real-space imaging of magnetic textures, but it generally has limited options for changing the magnetic field direction, usually confined to tilt angles of 45 degrees or less [21–23]. Yet, the in-plane component of the external magnetic field, and its relative orientation to the in-plane crystal axes play an important role in stabilizing antiskyrmion spin textures in MPS and FNPP, by first nucleating so-called non-topological bubble state [21, 24–27].

Resonant small-angle X-ray scattering (SAXS) is a reciprocal-space technique that probes similar lamellae samples but offers a more flexible magnetic field environment [28]. Modern synchrotron-based setups provide full three-dimensional vector-field control, enabling studies in geometries inaccessible to LTEM. Previous works have largely examined FNPP lamellae aligned along the c axis or in perpendicular and tilted fields, leaving the response to purely in-plane fields unexplored. Moreover, the interplay between basal magnetocrystalline anisotropy, anisotropic exchange interaction (AEI) [29], and the anisotropic DMI inherent to the S_4 symmetry has not yet been addressed.

Here, we employ element-selective resonant SAXS under vector magnetic fields and x-ray ptychography to address these open questions. By applying in-plane vector fields of controlled magnitude and direction within the (001) plane, we map the orientation and magnitude of the magnetic modulation vector **q** in FNPP over a broad temperature range (20–300 K) using SAXS. We find that at room temperature, the propagation vector of magnetic stripe domains can be continuously rotated by weak in-plane fields of about 10 mT, demonstrating full vectorial control of stripe orientation within the basal plane. In this regime, the Zeeman energy competes with and eventually overcomes the Dzyaloshinskii–Moriya interaction that stabilizes the chiral modulation, driving a transition from stripe domains to an achiral fan state. Upon cooling to 50 K and below, a weak fourfold anisotropy emerges, leading to spontaneous locking of the modulation direction to the field-training axis even after field removal. The temperature evolution is quantitatively reproduced by a theoretical model incorporating DMI, magnetocrystalline square anisotropy, and anisotropic exchange, which together establish an effective temperature-dependent basal-plane anisotropy governing the stripe-domain orientation.

2 | Results and Discussion

2.1 | Magnetic Textures in Zero and Out-of-plane Fields

FNPP crystallizes in tetragonal structure with the unit cell ($a = 9.1201(6)$ Å and $c = 4.4907(3)$ Å) as schematically shown in Figure 1a with the ground state magnetic modulation confined to the ⟨110⟩ crystal axes [10]. SAXS patterns measured at zero field show that the stripe domain state manifests as four magnetic Bragg peaks corresponding to two symmetry-equivalent directions (Figure 1b). The real-space period is $\lambda_0 = 234 \pm 3$ nm. Notably, even at zero field, SAXS reveals not only the first-order harmonics ($1q$) but also third-order ones ($3q$), while the second order is suppressed. Similar zero-field x-ray scattering patterns featuring third-order harmonics were also observed in MPS [17], Co/Pt multilayers [30], and from surface of Cu_2OSeO_3 [31]. The observation of pronounced third-order scattering indicates a strongly non-sinusoidal stripe (or π-CSL) modulation, consistent with sharp domain walls observed in the real-space ptychographic images (Figure 1f), which can be viewed as a distorted square-wave-like magnetic profile.

16163028, 2026, 79, Downloaded from https://advanced.onlinelibrary.wiley.com/doi/10.1002/adfm.77809 by Helmholtz-Zentrum Berlin Für, Wiley Online Library on [13/10/2026]. See the Terms and Conditions (https://onlinelibrary.wiley.com/terms-and-conditions) on Wiley Online Library for rules of use; OA articles are governed by the applicable Creative Commons License

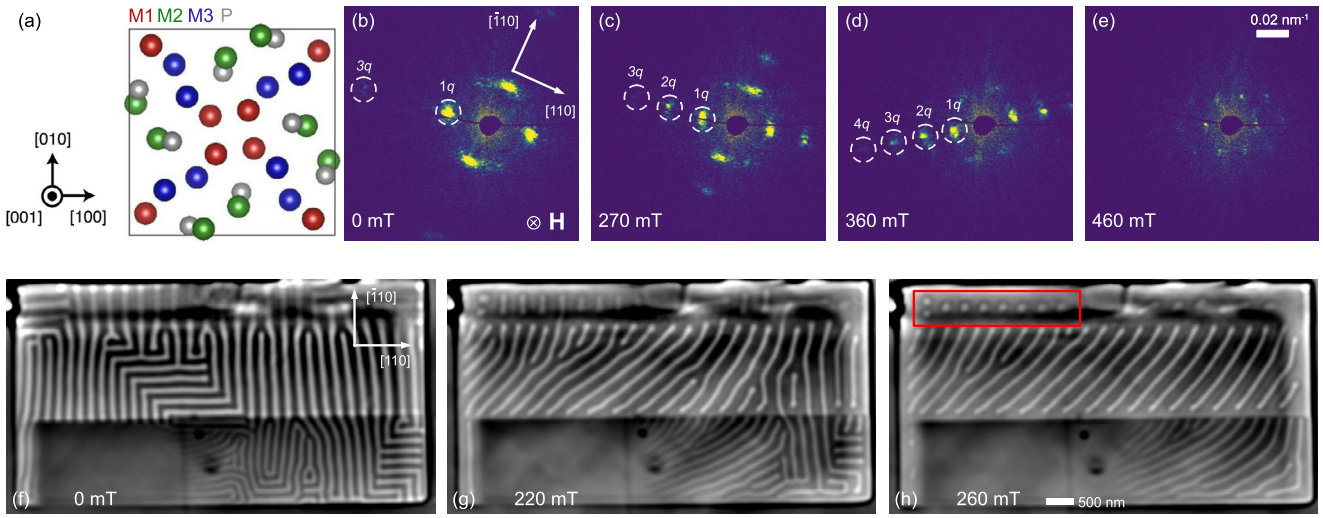

FIGURE 1 | (a) Schematic of noncentrosymmetric tetragonal crystal structure of $(Fe_{0.63}Ni_{0.3}Pd_{0.07})_3P$ viewed from [001] direction. Three inequivalent crystallographic sites, randomly occupied by metallic ions, are denoted M1, M2, and M3. (b–e) Resonant SAXS patterns measured in (b) zero field, (c) 270 mT, (d) 360 mT, and (e) 460 mT applied along the *c*-axis. (f–h) Real-space ptychographic phase images of magnetic textures measured at the out-of-plane magnetic field **H**||[001] of (f) 0 mT, (g) 220 mT, (h) 260 mT in stripe, soliton, and co-existing soliton and skyrmion states. Skyrmions nucleated at 260 mT are highlighted by the red box.

The slight departure of one of the zero-field stripe domains' orientation away from the crystal [$\bar{1}$10] axis is, most likely, influenced by the edge of the lamella (see Figure S1 given in Note S1). Upon increasing the magnetic field parallel to the *c* axis, SAXS reveals transitions from a multidomain chiral stripe-domain state (Figure 1b) into a soliton-lattice state with multiple higher harmonics up to 4th order (Figure 1c,d). Finally, a single-domain hexagonal skyrmion lattice (Figure 1e) is formed which is evidenced by a characteristic sixfold scattering pattern with weaker higher harmonics [32–35]. Above ~480 mT, the twisted texture unwinds, and the SAXS signal vanishes. Just before saturation, the modulation period increases by ~30% with respect to zero field ($\lambda = 340 \pm 3$ nm). Ptychographic phase images reconstructed from the SAXS signal of another FNPP lamella with distinct thickness steps from ~ 50 nm to ~ 200 nm are shown in Figures 1f–h. Stripes, solitons, and first skyrmion nucleation in the thicker part of the lamella are clearly reproduced. The increase of the period of magnetic textures with thickness and the sequence of transitions, correspond well with the magnetic phase diagram obtained previously by LTEM [10].

2.2 | Element-Selective Spectroscopy

By tuning the photon energy to the $L_{2,3}$ absorption edges of different transition metals, one can obtain element-selective information on the magnetization of each sublattice. Here, X-ray magnetic circular dichroism (XMCD) and SAXS were used to probe the magnetic ordering of Fe and Ni in FNPP, independently.

XMCD spectra (Figure 2a,b) measured in transmission geometry in the field-polarized state at the field $\mu_0 H = 500$ mT applied along the *c*-axis show strong magnetic contrast at both Fe and Ni $L_{2,3}$ edges. The same signs of the XMCD signal for both elements indicate parallel alignment of their moments. The presence of finite XMCD at the Ni edge is remarkable, as Ni_3P compound is paramagnetic [36], i.e., Ni carries only field-induced, spatially uncorrelated magnetic moments that do not participate in the long-range modulated magnetic structure. However, element-resolved SAXS maps (Figure 2c), measured at zero field, display coincident magnetic Bragg peaks at the same finite wavevector q at both the Fe (706.5 eV) and Ni (851.3 eV) resonances. A purely paramagnetic contribution would result only in a uniform ($q = 0$) magnetization and cannot produce scattering at finite q. The observation of identical scattering patterns therefore demonstrates that the Ni moments are spatially modulated and phase-locked to the Fe magnetic structure. This rules out a purely paramagnetic origin of the XMCD signal at the Ni edge and instead indicates that Ni carries an induced magnetic moment via proximity to Fe within the magnetically ordered state.

All subsequent SAXS measurements were performed at the Fe L_3 edge (706.5 eV), where the magnetic satellite intensity is maximized.

2.3 | Vector-Field Control of Stripe Domain Orientation

A key advantage of SAXS is the availability of a vector magnetic field at VEKMAG. In previous studies, the magnetic wavevector control in MPS by an ex situ in-plane field training [37], and in FNPP by a mechanical strain [38] has been demonstrated. Vector-field SAXS provides direct insights into the magnetic domain anisotropy. The response of the stripes to in-plane magnetic fields applied at an in-plane angle θ is shown in Figure 3. SAXS patterns were recorded while rotating the in-plane magnetic field azimuthally in 3° steps; $\theta = 0$ corresponds to the vertical direction in the laboratory reference system.

Individual SAXS patterns for the in-plane field **H** ∥ [100] crystal axis are shown in the Note S2. Summing the individual azimuthal

16163028, 2026, 79, Downloaded from https://advanced.onlinelibrary.wiley.com/doi/10.1002/adfm.77869 by Helmholtz-Zentrum Berlin Für, Wiley Online Library on [13/10/2026]. See the Terms and Conditions (https://onlinelibrary.wiley.com/terms-and-conditions) on Wiley Online Library for rules of use; OA articles are governed by the applicable Creative Commons License

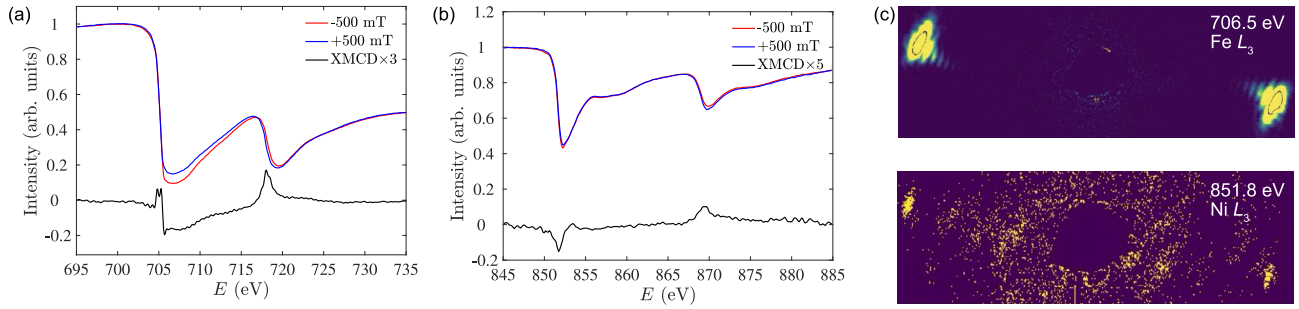

FIGURE 2 | (a,b) Soft x-ray transmission and XMCD spectra measured across Fe and Ni $L_{2,3}$ edges, respectively. (c) Rescaled element-selective SAXS patterns measured at zero field at Fe and Ni edges.

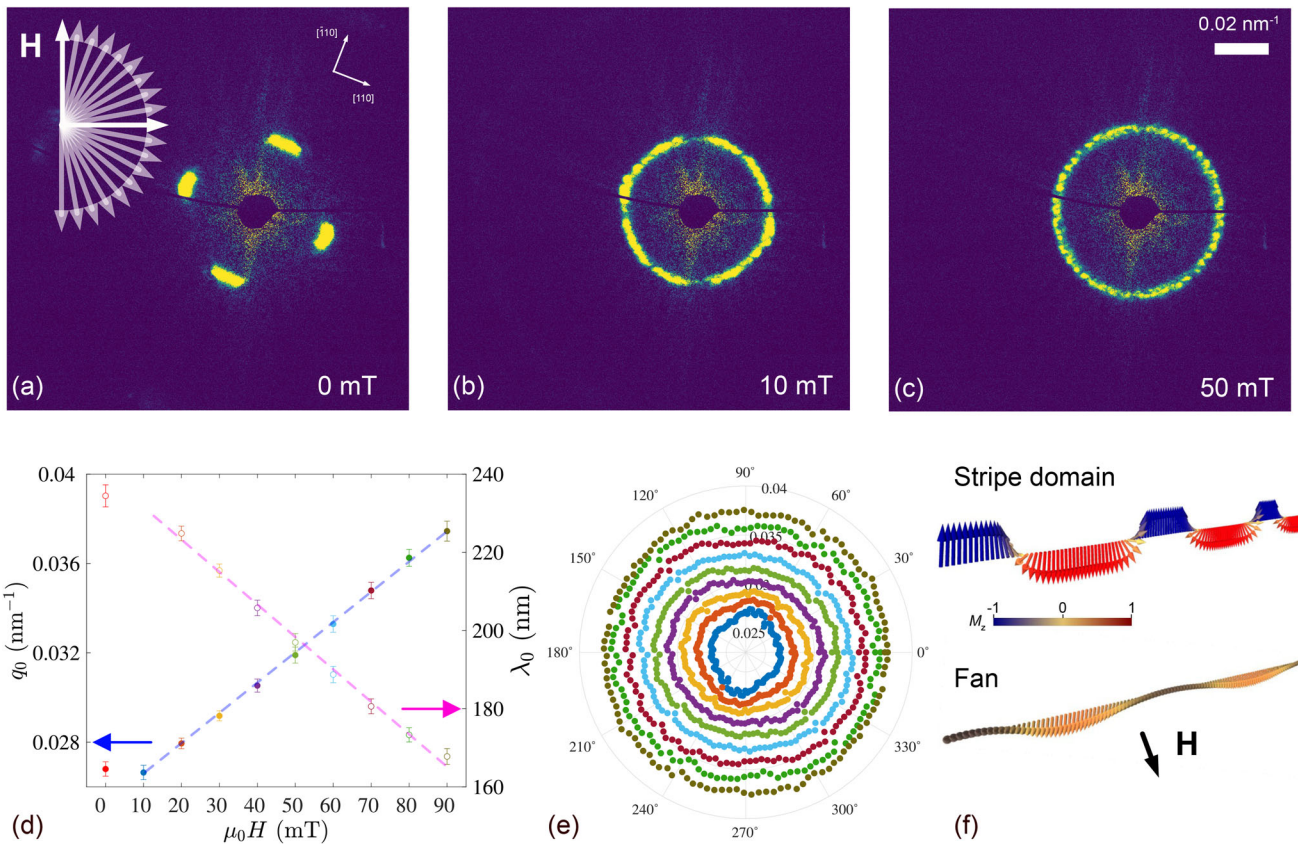

FIGURE 3 | Summed vector-field SAXS patterns measured at 300 K and at the magnitude of the azimuthal magnetic field of (a) 0 mT, (b) 10 mT, and (c) 50 mT. (d) In-plane field dependence of the magnetic wavevector and the corresponding real-space stripe periodicity averaged over all azimuthal field angles. (e) Polar plot of the wavevector magnitude as a function of the azimuthal field angle and the magnitude of the field. Symbol colors correspond to those indicating the field magnitudes in panel (d). (f) Schematics of zero-field stripe domain and in-plane field-induced fan structures.

SAXS maps measured at 300 K for field amplitudes of 0, 10, and 50 mT results in the patterns shown in Figure 3a–c. The averaged SAXS pattern at zero magnetic field reveals that the magnetic propagation vectors are pinned along [110] and [$\bar{1}$10] due to anisotropic DMI favoring the Bloch domain walls in these directions. Néel structures, which can in principle emerge in [100] and [010] directions, are strongly suppressed by the magnetostatic energy (see Note S3 for details). A weak in-plane field of 10 mT collapses the intensity into a pair of spots perpendicular to the field, indicating that **q** aligns normal to **H**. Thus, even a weak external magnetic field of 10 mT is sufficient to align the domains in any in-plane direction, overcoming the anisotropic effect of DMI. This also indicates weak basal-plane square anisotropy and anisotropic exchange.

Upon further increasing the in-plane field, the system undergoes a transition from the chiral stripe state to an achiral fan-like configuration, as illustrated in Figure 3f. This transition occurs when the Zeeman energy gain of the fan state overcomes the DMI-induced chiral twisting (see Note S3 for details). The

16163028, 2026, 79, Downloaded from https://advanced.onlinelibrary.wiley.com/doi/10.1002/adfm.77809 by Helmholtz-Zentrum Berlin Für, Wiley Online Library on [13/10/2026]. See the Terms and Conditions (https://onlinelibrary.wiley.com/terms-and-conditions) on Wiley Online Library for rules of use; OA articles are governed by the applicable Creative Commons License

corresponding critical field is given by

$$H_C = \frac{M_s \gamma}{\sqrt{\alpha/\beta}}, \quad (1)$$

where M_s is the magnetization modulus at a given temperature, α is the exchange stiffness, β – perpendicular anisotropy, and γ is the effective DMI strength. Evidently, $\sqrt{\alpha/\beta}$ corresponds to the well-known domain wall width. Using parameter values from Ref. [10], we estimate a transition field of approximately 30 mT (see Note S3). Above this field, and in the absence of significant basal-plane anisotropy, the modulation wavevector becomes isotropic, as the influence of DMI on its orientation is effectively suppressed. This behavior is consistent with our experimental observations shown in Figure 3e.

Increasing the magnetic field amplitude to 90 mT reduces the stripe period to $\lambda_0 = 167 \pm 3$ nm (see Figure 3d), in contrast to the **H** ∥ [001] geometry, and consistent with systems combining DMI and easy-axis anisotropy [39]. After removing the field, the original domain orientations are restored, with **q** vectors pinned along the ⟨110⟩ directions, analogous to the behavior in Cu_2OSeO_3 under vectorial fields [28, 40].

Polar plots of **q** (Figure 3e) show a continuous rotation of the stripe orientation with the azimuthal field direction. At room temperature, the **q** distribution is isotropic in the (001) plane and reflects neither the crystal symmetry nor the sample shape. In contrast to cubic chiral magnets, where the symmetry-allowed conical state constrains the field response, in FNPP the absence of such a conical phase permits an arbitrary reorientation of the in-plane modulation vector via a fan state.

To summarize, at room temperature, we observe the following scenario for the in-plane field-induced transitions: in the range of magnetic fields < 10 mT, related to the scale of the anisotropic DMI, chiral Bloch stripe structures with pinned directions are stabilized. Weak magnetic fields $\gtrsim$ 10 mT lead to orientation of the stripe **q**-vectors perpendicular to the field direction and transform them into nonchiral fan structures, see Figure 3f. Notably, in this regime, the effective role of anisotropic DMI in forming the chiral domain texture is suppressed, and basal-plane anisotropy is negligible; hence, the stripe domain structure period is nearly isotropic. Upon further in-plane field increase, the domain wall energy drops down [39] and the period decreases (see also Note S3). The stripe domains progressively transition into a fan-like structure. This transformation scenario is also supported by micromagnetic simulations presented in the see Figure S4. A comprehensive micromagnetic study into the mechanism underlying the stripe-to-fan transformation is presented in a separate study on MPS [41].

2.4 | Temperature Evolution and Basal-Plane Anisotropy

Upon cooling, the vectorial magnetic field control of **q** changes drastically. At 50 K, zero-field alignment of domains by field training becomes possible. Figure 4a presents SAXS intensity distributions at zero field after applying and removing an in-plane field at various temperatures. At 100 K and above, **q** reverts to ⟨110⟩ after field removal, whereas at 50 K and below the stripes retain the trained orientation, revealing metastable directional memory. This behavior resembles directional pinning of helices observed in chiral FeGe [29] and $Co_8Zn_8Mn_4$ [42], and is similar to the low-temperature state in MPS below the spin-reorientation transition [37].

The energy of Bloch-type stripe domains depends on their orientation through anisotropic DMI and basal-plane anisotropy, leading to an angular variation of the stripe wavevector $q(\theta)$. Polar plots of $q(\theta)$ (Figure 4b) reveal a clear fourfold anisotropy at 50 K, while more complex shapes are observed at lower temperatures.

To quantify this behavior, we model $q(\theta)$ using a phenomenological approach that perturbatively incorporates the DMI, an effective basal-plane anisotropy, and a strain-induced in-plane uniaxial anisotropy. The effective basal anisotropy combines magnetocrystalline square anisotropy and anisotropic exchange interaction (AEI), which cannot be disentangled within the present experimental sensitivity. The uniaxial term arises naturally from the lamella preparation by Focused Ion Beam (FIB), where the sample is mounted onto a silicon nitride membrane using Pt contacts (see Figure S1c). This introduces residual strain, which is further enhanced upon cooling due to thermal expansion mismatch and is known to influence magnetic textures. The role of strain in chiral magnets has been widely demonstrated, including x-ray studies on Cu_2OSeO_3 [43] and FeGe [34], as well as LTEM investigations of $Co_8Zn_{8.5}Mn_{3.5}$ [44] and FNPP [38]. In FNPP specifically, strain has been shown to modify stripe-domain orientation even at zero field [38].

Within this framework, the characteristic wavevector can be expressed as

$$q(\theta) = q_0 \Big[1 + b \sin^2(\theta - \theta_S) + d|\cos 2(\theta - \theta_D)| + f \sin^2 2\theta \Big] \quad (2)$$

where $b \sim \beta_S/\beta$ accounts for the strain-induced anisotropy, $d \sim \gamma/\sqrt{\alpha\beta}$ quantifies the DMI contribution, f represents the effective basal anisotropy (see Note S3). Here, γ is the DMI constant, α is the exchange stiffness, β and β_S are for perpendicular and in-plane strain-induced axial anisotropies. Angles θ_D and θ_S indicate the orientations of the DMI and strain axes, respectively.

For the 20 K data, the fitted model yields $d \approx 0.073 \pm 0.019$ and $b \approx -0.023 \pm 0.015$. These parameters are nearly temperature-independent and remain within the experimental uncertainty. In contrast, the effective anisotropy parameter f increases by an order of magnitude upon cooling from 50 K to 20 K, changing from negligible $f = 0.001 \pm 0.006$ to significant $f = -0.070 \pm 0.015$. This strong enhancement is consistent with previous ferromagnetic resonance measurements on bulk FNPP [19] and general expectations, since higher-order magnetocrystalline anisotropy scales with higher powers of magnetization and anisotropic exchange becomes more prominent as thermal fluctuations are suppressed [28, 42]. In addition, the random occupation of Fe, Ni, and Pd sites, combined with the strong spin–orbit coupling of Pd, may give rise to locally varying anisotropies that become increasingly relevant at low temperatures. Moreover, the

16163028, 2026, 79, Downloaded from https://advanced.onlinelibrary.wiley.com/doi/10.1002/adfm.77869 by Helmholtz-Zentrum Berlin Für, Wiley Online Library on [13/10/2026]. See the Terms and Conditions (https://onlinelibrary.wiley.com/terms-and-conditions) on Wiley Online Library for rules of use; OA articles are governed by the applicable Creative Commons License

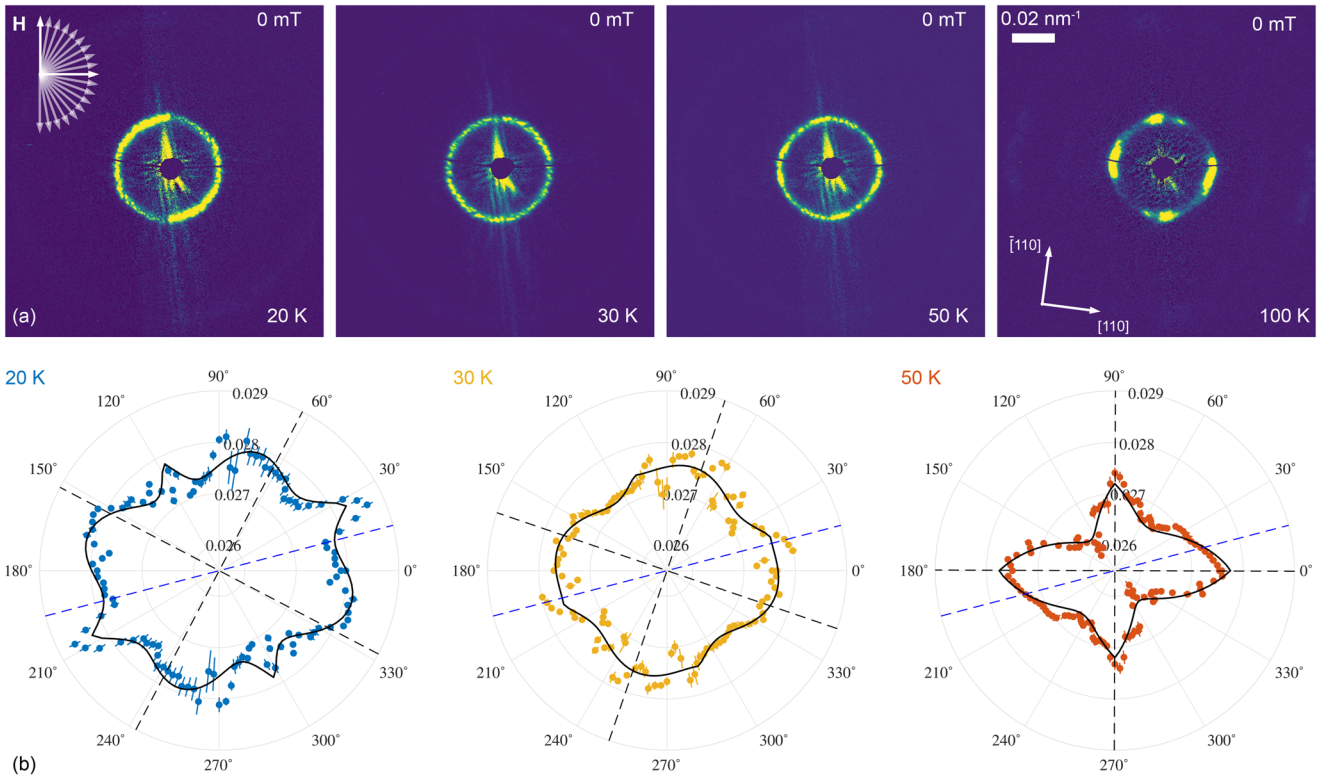

FIGURE 4 | (a) Summed zero-field SAXS patterns measured at 20, 30, 50, 100 K after applying a saturating field of 200 mT in every azimuthal direction with a 3° step. At 100 K and above, the domain propagation direction always returns to its original axis. (b) Polar plot of the magnetic wavevector magnitude as a function of the azimuthal field angle at 20, 30, and 50 K at zero field. Solid curves represent the fit according to the theoretical model discussed in the main text. Dashed black lines indicate the fitted orientations of the effective DMI axes, while the dashed blue line marks the direction of the in-plane uniaxial strain.

contribution of the square magnetocrystalline anisotropy scales with the square of the magnetization, leading to a temperature-dependent correction of order $\sim (T/T_C)^{3/2}$ for $T \ll T_C$. This implies that the conventional enhancement of the basal-plane anisotropy due to the increase of the saturated magnetization upon cooling from 50 K to 20 K is limited to approximately 10%, and therefore cannot account for the pronounced experimentally observed growth. In contrast, a substantial increase of the AEI at temperatures well below the ordering temperature has been reported for cubic helimagnets [28, 29], suggesting that AEI provides a more plausible microscopic origin for the strong low-temperature enhancement of the basal anisotropy.

At 50 K, where the basal anisotropy remains relatively weak, the DMI term produces a cusp-like angular dependence of $q(\theta)$ near the ⟨110⟩ directions, while the strain-induced contribution introduces a small asymmetry between otherwise equivalent axes (the strain direction is indicated in Figure 4b). Upon further cooling, we observe a systematic rotation of the effective DMI axis θ_D by approximately 20° at 30 K and 30° at 20 K. Such a rotation is not symmetry-forbidden for the S_4 group and points to a temperature-dependent renormalization of the DMI tensor. Microscopically, this may originate from a weak symmetry lowering within the basal plane-e.g., toward an orthorhombic distortion—driven by magnetoelastic coupling or differential thermal contraction, which modifies the underlying spin–orbit–coupled exchange paths. In addition, the progressive freezing of spin and phonon fluctuations can further renormalize the balance of competing anisotropic interactions. These results provide experimental evidence that in complex tetragonal magnets the effective DMI orientation need not be rigidly symmetry-locked, but can evolve with temperature. A quantitative understanding of this effect will require microscopic modeling, for instance based on temperature-dependent ab initio calculations of the anisotropic interactions.

Overall, the evolution from nearly isotropic behavior at high temperatures to pronounced fourfold (50–30 K) and eventually more complex anisotropy at 20 K reflects a temperature-dependent competition between DMI, strain, and basal-plane anisotropies. While DMI governs the preferred modulation directions at elevated temperatures, the increasing strength of magnetocrystalline and exchange anisotropies at low temperatures distorts the angular dependence and stabilizes specific domain orientations.

3 | Conclusion

We have investigated magnetic stripe domains in noncentrosymmetric $(Fe_{0.63}Ni_{0.3}Pd_{0.07})_3P$ using element-selective resonant soft x-ray scattering and spectroscopy under vector magnetic fields, in addition to imaging topological magnetic textures in real space by soft x-ray ptychography. The element selectivity of soft x-rays reveals an induced magnetic moment in Ni, which is absent in the parent compound Ni_3P, confirming a strong exchange coupling between the Fe and Ni sublattices. At room temperature,

16163028, 2026, 79, Downloaded from https://advanced.onlinelibrary.wiley.com/doi/10.1002/adfm.77809 by Helmholtz-Zentrum Berlin Für, Wiley Online Library on [13/10/2026]. See the Terms and Conditions (https://onlinelibrary.wiley.com/terms-and-conditions) on Wiley Online Library for rules of use; OA articles are governed by the applicable Creative Commons License

the magnetic modulation vector can be continuously rotated by weak in-plane fields of only a few millitesla, demonstrating nearly isotropic modulation within the basal plane. Upon cooling below 50 K, a fourfold basal-plane anisotropy emerges, and the stripe-domain orientation becomes metastably pinned along the direction of the previously applied field. Notably, we observed and quantified the temperature evolution of effective DMI orientation caused by a competition of two symmetry-allowed contributions of different origin.

Furthermore, we develop a closed analytical description of the stripe-to-fan transition under in-plane fields that incorporates anisotropic DMI together with basal anisotropy, yielding a quantitative expression for the critical field that governs the stability and reorientation of chiral stripe domains. This provides the first explicit analytical framework linking DMI, anisotropic exchange, and vector-field-driven domain reconfiguration in tetragonal noncentrosymmetric magnets.

Our results show that FNPP hosts a competition between nearly isotropic and anisotropic magnetic interactions, enabling vector-field control of magnetic domain orientation and directional memory effects at cryogenic temperatures. Rather than establishing FNPP as a generic model system, our findings identify a concrete mechanism by which weak in-plane fields reorganize chiral stripe states through a DMI-anisotropy-Zeeman balance. More broadly, these results demonstrate how vector magnetic fields can be used to manipulate mesoscale magnetic textures in noncentrosymmetric magnets, providing a route toward controllable topological spin structures in functional magnetic materials.

4 | Experimental Section

4.1 | Samples

Single crystals of $(Fe_{0.63}Ni_{0.3}Pd_{0.07})_3P$ were grown by a self-flux method and characterized as described previously [10]. The crystals were oriented by Laue diffraction, and a thin (~120 nm) (001)-oriented lamella for transmission x-ray measurements was prepared by focused ion beam (FIB) milling. The lamella was attached to a masked Si_3N_4 membrane (Silson Ltd., UK) with a 5 μm circular pinhole using two Pt contacts. Details of similar sample preparation routines and associated challenges are discussed in Refs. [34, 45]. LTEM and scanning electron microscopy (SEM) images of the lamella before and after its deposition on a membrane are shown in the Note S1.

4.2 | Resonant Small-Angle X-Ray Scattering and Spectroscopy

Resonant SAXS measurements in vectorial magnetic fields were performed at the PM-2 VEKMAG [46], and preliminary SAXS data was acquired at PM-3 ALICE II endstation of the BESSY II synchrotron (Berlin, Germany). At both instruments circularly polarized soft x-ray beam with the size of 100 μ were tuned to the Fe and Ni L_3 edges. The FNPP lamella was oriented perpendicular to the x-ray beam. Details of the VEKMAG setup for SAXS measurements are provided in Refs. [28, 29, 42]. In particular, VEKMAG allows for soft x-ray spectroscopy and SAXS measurements in vectorial magnetic field: a 9/2/1 T cryomagnet equipped with three superconducting coils provides independent control of the magnetic field components, resulting in up to 1 T in any spatial direction. The acquisition time per SAXS pattern was 20 s. An image containing only the charge scattering was taken at the saturating field of 0.5 T, and subtracted as background.

Sample alignment and energy-dependent x-ray spectra were recorded using a transmission photodiode. X-ray magnetic circular dichroism (XMCD) data were collected in oppositely saturated magnetic states at $\mu_0 H = \pm 0.5$ T in normal geometry.

4.3 | Soft X-Ray Ptychography

Soft x-ray ptychography measurements [47], which allow nanoscale imaging of noncollinear magnetic order by reconstruction of resonant x-ray scattering [48], were carried out at the MAXYMUS microscope at BESSY II. The experiment was performed at room temperature in an out-of-plane magnetic field up to 260 mT provided by a system based on permanent magnets [49]. Ptychographic images were obtained at the Fe L_3 pre-edge (1 eV below the absorption maximum to enhance the phase contrast) with circularly polarized x-rays, using an inverse low-gain avalanche diode (iLGAD) Eiger soft-x-ray detector with 512×512 pixels (75 μm pixel size) [50]. The distance between the sample and the detector was 76 mm. An exposure time of 200 ms was used to record diffraction patterns from 100 nm spaced areas illuminated by a 900 nm full width at half maximum (FWHM) x-ray spot, which was shaped by a 320 μm diameter Fresnel zone plate with 18 nm outer zone width. Ptychographic reconstructions were carried out with the difference-map [51] and maximum-likelihood methods [52] as implemented in the PtychoShelves software [53].

Author Contributions

K.K., Y. To., Y. Ta. prepared and characterized single crystals; V.U., L.U., C.L., R.A., P.W., F.R. performed x-ray scattering measurements; V.U., C.L., T.A.B., S.F., S.W., M.We. carried out x-ray ptychography measurements, V.U., H.K., M.Wi., S.S., A.T., B.R., M.B. prepared lamellae samples; O.I.U. and V.U. developed the theory and performed simulations; V.U., O.I.U. wrote the manuscript; V.U., K.K. and F.R. jointly conceived the project.

Acknowledgments

REXS experiments were carried out the BESSY II synchrotron as a part of proposals Photons-232-12305-ST, 232-12260-ST and 242-12606-EF. We thank the Helmholtz–Zentrum Berlin für Materialien und Energie for the allocation of beamtime at VEKMAG, ALICE II and MAXYMUS instruments. We thank R. Zehmke and T. Kachel for technical support. We thank M. Rahn, A. Sukhanov and J. Masell for fruitful discussions.

We thank the CoreLab Correlative Microscopy and Spectroscopy at Helmholtz–Zentrum Berlin, and Dresden Center for Nanoanalysis for the sample preparation using FIB.

We thank E. Fröjdh, F. Baruffaldi, M. Carulla, J. Zhang, and A. Bergamaschi of the Detector Group of the Paul Scherrer Institute (Villigen, Switzerland) Center for Photon Science for the development and provision of the iLGAD EIGER detector. The iLGAD sensors were fabricated at Fondazione Bruno Kessler (Trento, Italy).

The authors acknowledge financial support for the VEKMAG project and for the PM2-VEKMAG beamline by the German Federal Ministry for

16163028, 2026, 79, Downloaded from https://advanced.onlinelibrary.wiley.com/doi/10.1002/adfm.77869 by Helmholtz-Zentrum Berlin Für, Wiley Online Library on [13/10/2026]. See the Terms and Conditions (https://onlinelibrary.wiley.com/terms-and-conditions) on Wiley Online Library for rules of use; OA articles are governed by the applicable Creative Commons License

Education and Research (BMBF 05K2010, 05K2013, 05K2016, 05K2019) and by HZB. The study was also supported by JST CREST (Grant No. JPMJCR20T1), and the RIKEN TRIP initiative (Many-body Electron Systems and Advanced General Intelligence for Science Program). F.R. acknowledges funding by the German Research Foundation via Project No. SPP2137/RA 3570. O.I.U. acknowledges financial support from the Brain Pool Plus Program through the National Research Foundation of Korea funded by the Ministry of Science and ICT (2020H1D3A2A03099291). T.A.B. acknowledges funding from the European Regional Development Fund (ERDF). K.K. acknowledges financial support from the Japan Society for the Promotion of Science (KAKENHI, Grant No. 23K26534) and from the Japan Science and Technology Agency through the FOREST Program (Grant No. JPMJFR235R). M.W. acknowledges support from the International Max Planck Research School for Chemistry and Physics of Quantum Materials (IMPRS-CPQM). M.W., S.S., and B.R. are grateful for funding from the DFG through SPP 2137, project no. 403503416.

Open access funding enabled and organized by Projekt DEAL.

Conflicts of Interest

The authors declare no conflicts of interest.

Data Availability Statement

The data that support the findings of this study are available from the corresponding author upon reasonable request.

References

1. P. Bak and M. H. Jensen, "Theory of Helical Magnetic Structures and Phase Transitions in MnSi and FeGe," *Journal of Physics C: Solid State Physics* 13, no. 31 (1980): L881.

2. A. Bogdanov and A. Hubert, "Thermodynamically Stable Magnetic Vortex States in Magnetic Crystals," *Journal of Magnetism and Magnetic Materials* 138, no. 3 (1994): 255–269.

3. I. Dzyaloshinsky, "A Thermodynamic Theory of "Weak" Ferromagnetism of Antiferromagnetics," *Journal of Physics and Chemistry of Solids* 4, no. 4 (1958): 241–255.

4. T. Moriya, "Anisotropic Superexchange Interaction and Weak Ferromagnetism," *Physical Review* 120, no. 1 (1960): 91.

5. S. Mühlbauer, B. Binz, F. Jonietz, C. Pfleiderer, A. Rosch, A. Neubauer, R. Georgii, and P. Böni, "Skyrmion Lattice in a Chiral Magnet," *Science* 323, no. 5916 (2009): 915–919.

6. Y. Tokunaga, X. Z. Yu, J. S. White, et al., "A New Class of Chiral Materials Hosting Magnetic Skyrmions beyond Room Temperature," *Nature Communications* 6, no. 1 (2015): 7638.

7. I. Kézsmárki, S. Bordács, P. Milde, et al., "Néel-Type Skyrmion Lattice with Confined Orientation in the Polar Magnetic Semiconductor GaV_4S_8," *Nature Materials* 14, no. 11 (2015): 1116–1122.

8. T. Kurumaji, T. Nakajima, V. Ukleev, et al., "Néel-Type Skyrmion Lattice in the Tetragonal Polar Magnet $VOSe_2O_5$," *Physical Review Letters* 119, no. 23 (2017): 237201.

9. A. K. Nayak, V. Kumar, T. Ma, et al., "Magnetic Antiskyrmions above Room Temperature in Tetragonal Heusler Materials," *Nature* 548, no. 7669 (2017): 561–566.

10. K. Karube, L. Peng, J. Masell, et al., "Room-Temperature Antiskyrmions and Sawtooth Surface Textures in a Non-Centrosymmetric Magnet with S_4 Symmetry," *Nature Materials* 20, no. 3 (2021): 335–340.

11. K. Karube and Y. Taguchi, "High-Temperature Non-Centrosymmetric Magnets for Skyrmionics," *APL Materials* 10, no. 8 (2022): 080902.

12. N. Mukai and A. O. Leonov, "Skyrmion and Meron Ordering in Quasi-Two-Dimensional Chiral Magnets," *Physical Review B* 106, no. 22 (2022): 224428.

13. T. Ma, A. K. Sharma, R. Saha, et al., "Tunable Magnetic Antiskyrmion Size and Helical Period from Nanometers to Micrometers in a D_{2d} Heusler Compound," *Advanced Materials* 32, no. 28 (2020): 2002043.

14. A. Sukhanov, B. Z. Cespedes, P. Vir, et al., "Anisotropic Fractal Magnetic Domain Pattern in Bulk $Mn_{1.4}PtSn$," *Physical Review B* 102, no. 17 (2020): 174447.

15. K. Karube, V. Ukleev, F. Kagawa, Y. Tokura, Y. Taguchi, and J. S. White, "Unveiling the Anisotropic Fractal Magnetic Domain Structure in Bulk Crystals of Antiskyrmion Host $(Fe,Ni,Pd)_3P$ by Small-Angle Neutron Scattering," *Journal of Applied Crystallography* 55, no. 6 (2022): 1392–1400.

16. A. Hubert and R. Schäfer, *Magnetic Domains: The Analysis of Magnetic Microstructures* (Springer Science & Business Media, 1998).

17. M. Winter, A. Pignedoli, M. C. Rahn, et al., "Field-Induced Condensation of π to 2π Soliton Lattices in Chiral Magnets," *Communications Physics* 9, no. 264 (2026), https://doi.org/10.1038/s42005-026-02785-3.

18. K. Karube, L. Peng, J. Masell, et al., "Doping Control of Magnetic Anisotropy for Stable Antiskyrmion Formation in Schreibersite $(Fe,Ni)_3P$ with S_4 Symmetry," *Advanced Materials* 34, no. 11 (2022): 2108770.

19. M. Hemmida, J. Masell, K. Karube, et al., "Role of Magnetic Anisotropy in the Antiskyrmion-Host Schreibersite Magnets," *Physical Review B* 110, no. 5 (2024): 054416.

20. S. Mühlbauer, D. Honecker, É. A. Périgo, et al., "Magnetic Small-Angle Neutron Scattering," *Reviews of Modern Physics* 91, no. 1 (2019): 015004.

21. L. Peng, R. Takagi, W. Koshibae, et al., "Controlled Transformation of Skyrmions and Antiskyrmions in a Non-Centrosymmetric Magnet," *Nature Nanotechnology* 15, no. 3 (2020): 181–186.

22. J. Jena, B. Göbel, T. Ma, et al., "Elliptical Bloch Skyrmion Chiral Twins in an Antiskyrmion System," *Nature Communications* 11, no. 1 (2020): 1115.

23. Z. He, Z. Wang, Z. Li, et al., "Manipulation of Topological Antiskyrmion Lattice Transition at Room Temperature," *Advanced Functional Materials* 36 (2026): e31037.

24. L. Peng, K. V. Iakoubovskii, K. Karube, Y. Taguchi, Y. Tokura, and X. Yu, "Formation and Control of Zero-Field Antiskyrmions in Confining Geometries," *Advanced Science* 9, no. 28 (2022): 2202950.

25. J. Tang, Y. Wu, J. Jiang, et al., "Sewing Skyrmion and Antiskyrmion by Quadrupole of Bloch Points," *Science Bulletin* 68, no. 23 (2023): 2919–2923.

26. T. Muto and M. Mochizuki, "Switching Magnetic Texture via In-Plane Magnetic Field in Noncentrosymmetric Dipolar Magnets: From Skyrmions to Antiskyrmions and Nontopological Magnetic Bubbles," *Physical Review B* 112, no. 10 (2025): 104409.

27. Y. Wu, J. Jiang, L. Kong, et al., "Current-Controlled Creations, Deletions, and Topological Transformations of a Single Magnetic Antiskyrmion in Nanostructured Cells," *Nature Communications* 16 (2025): 11626.

28. P. R. Baral, O. I. Utesov, C. Luo, et al., "Direct Observation of Exchange Anisotropy in the Helimagnetic Insulator Cu_2OSeO_3," *Physical Review Research* 5 (2023): L032019.

29. V. Ukleev, O. Utesov, L. Yu, et al., "Signature of Anisotropic Exchange Interaction Revealed by Vector-Field Control of the Helical Order in a FeGe Thin Plate," *Physical Review Research* 3, no. 1 (2021): 013094.

30. O. Hellwig, G. Denbeaux, J. Kortright, and E. E. Fullerton, "X-Ray Studies of Aligned Magnetic Stripe Domains in Perpendicular Multilayers," *Physica B: Condensed Matter* 336, no. 1-2 (2003): 136–144.

31. P. R. Baral, O. I. Utesov, S. H. Moody, et al., "A Surface-Confined Spiral State with the Double Period in the Cubic Chiral Helimagnet Cu_2OSeO_3," *npj Quantum Materials* (2026), https://doi.org/10.1038/s41535-026-00892-6.

32. T. Adams, S. Mühlbauer, C. Pfleiderer, et al., "Long-Range Crystalline Nature of the Skyrmion Lattice in MnSi," *Physical Review Letters* 107, no. 21 (2011): 217206.

16163028, 2026, 79, Downloaded from https://advanced.onlinelibrary.wiley.com/doi/10.1002/adfm.77869 by Helmholtz-Zentrum Berlin Für, Wiley Online Library on [13/10/2026]. See the Terms and Conditions (https://onlinelibrary.wiley.com/terms-and-conditions) on Wiley Online Library for rules of use; OA articles are governed by the applicable Creative Commons License

33. E. Moskvin, S. Grigoriev, V. Dyadkin, et al., "Complex Chiral Modulations in FeGe Close to Magnetic Ordering," *Physical Review Letters* 110, no. 7 (2013): 077207–1.

34. V. Ukleev, Y. Yamasaki, O. Utesov, et al., "Metastable Solitonic States in the Strained Itinerant Helimagnet FeGe," *Physical Review B* 102, no. 1 (2020): 014416.

35. J. D. Reim, S. Matsuzaka, K. Makino, et al., "Higher-Order Modulations in the Skyrmion Lattice Phase of Cu_2OSeO_3," *Physical Review B* 106, no. 10 (2022): 104406.

36. R. Gambino, T. McGuire, and Y. Nakamura, "Magnetic Properties of the Iron-Group Metal Phosphides," *Journal of Applied Physics* 38, no. 3 (1967): 1253–1255.

37. A. Sukhanov, V. Ukleev, P. Vir, et al., "Hybrid Bloch-Néel Spiral States in $Mn_{1.4}PtSn$ Probed by Resonant Soft X-Ray Scattering," *Physical Review B* 106, no. 14 (2022): L140402.

38. S. Mori, S. Ii, T. Moronaga, et al., "Direct Observations of Mechanical Strain-Induced Wavevector Switching in a $(Fe,Ni,Pd)_3P$ Magnet with Anisotropic Dzyaloshinskii–Moriya Interaction," *ACS Applied Materials and Interfaces* 17, no. 15 (2025): 22921–22928.

39. S. Yang, K.-W. Moon, T.-S. Ju, C. Kim, S. Park, and C. Hwang, "Universality of Stripe Domain Width Change by an In-Plane Magnetic Field," *Journal of Magnetism and Magnetic Materials* 539 (2021): 168381.

40. S. Moody, P. Nielsen, M. Wilson, et al., "Experimental Evidence of a Change of Exchange Anisotropy Sign with Temperature in Zn-Substituted Cu_2OSeO_3," *Physical Review Research* 3, no. 4 (2021): 043149.

41. M. Winter, A. Pignedoli, A. S. Sukhanov, et al., "Quasi-1D Spin Textures: From Chiral Soliton Lattice to Fan State," *arXiv preprint arXiv:2606.21034* (2026).

42. V. Ukleev, O. I. Utesov, C. Luo, et al., "Competing Anisotropies in the Chiral Cubic Magnet $Co_8Zn_8Mn_4$ Unveiled by Resonant X-Ray Magnetic Scattering," *Physical Review B* 109, no. 18 (2024): 184415.

43. Y. Okamura, Y. Yamasaki, D. Morikawa, et al., "Emergence and Magnetic-Field Variation of Chiral-Soliton Lattice and Skyrmion Lattice in the Strained Helimagnet Cu_2OSeO_3," *Physical Review B* 96, no. 17 (2017): 174417.

44. H. Zhao, T.-H. Kim, L. Zhou, and L. Ke, "Controlling Skyrmion Lattices via Strain: Elongation, Tilting, and Collapse Mechanisms," *Physical Review B* 112, no. 21 (2025): 214417.

45. V. Ukleev, Y. Yamasaki, D. Morikawa, et al., "Element-Specific Soft X-Ray Spectroscopy, Scattering, and Imaging Studies of the Skyrmion-Hosting Compound $Co_8Zn_8Mn_4$," *Physical Review B* 99, no. 14 (2019): 144408.

46. T. Noll and F. Radu, "The Mechanics of the VEKMAG Experiment," *Proceedings of MEDSI2016, Barcelona, Spain* (2016): 370–373.

47. T. A. Butcher, S. Finizio, L. Heller, et al., "Soft X-Ray Ptychography with SOPHIE: Guide and Instrumentation," *Review of Scientific Instruments* 96, no. 12 (2025): 123704.

48. T. A. Butcher, N. W. Phillips, C.-C. Chiu, et al., "Ptychographic Nanoscale Imaging of the Magnetoelectric Coupling in Freestanding $BiFeO_3$," *Advanced Materials* 36, no. 23 (2024): 2311157.

49. D. Nolle, M. Weigand, P. Audehm, et al., "Note: Unique Characterization Possibilities in the Ultra High Vacuum Scanning Transmission X-Ray Microscope (UHV-STXM) "MAXYMUS" Using a Rotatable Permanent Magnetic Field up to 0.22 T," *Review of Scientific Instruments* 83, no. 4 (2012): 046112.

50. F. Baruffaldi, A. Bergamaschi, M. Boscardin, et al., "Single-Photon Counting Pixel Detector for Soft X-Rays," *Communications Physics* 8, no. 1 (2025): 321.

51. P. Thibault, M. Dierolf, A. Menzel, O. Bunk, C. David, and F. Pfeiffer, "High-Resolution Scanning X-Ray Diffraction Microscopy," *Science* 321, no. 5887 (2008): 379–382.

52. M. Odstrčil, A. Menzel, and M. Guizar-Sicairos, "Iterative Least-Squares Solver for Generalized Maximum-Likelihood Ptychography," *Optics Express* 26, no. 3 (2018): 3108–3123.

53. K. Wakonig, H.-C. Stadler, M. Odstrčil, et al., "PtychoShelves, a Versatile High-Level Framework for High-Performance Analysis of Ptychographic Data," *Journal of Applied Crystallography* 53, no. 2 (2020): 574–586.

Supporting Information

Additional supporting information can be found online in the Supporting Information section.

Supporting File: adfm77809-sup-0001-SuppMat.pdf.

16163028, 2026, 79, Downloaded from https://advanced.onlinelibrary.wiley.com/doi/10.1002/adfm.77809 by Helmholtz-Zentrum Berlin Für, Wiley Online Library on [13/10/2026]. See the Terms and Conditions (https://onlinelibrary.wiley.com/terms-and-conditions) on Wiley Online Library for rules of use; OA articles are governed by the applicable Creative Commons License